Aligned Growth of Hexagonal Boron Nitride Monolayer on Germanium

*Jun Yin, Xiaofei Liu, Wanglin Lu, Jidong Li, Yuanzhi Cao, Yao Li, Ying Xu, Xuemei Li, Jun Zhou, Chuanhong Jin, and Wanlin Guo**

Monolayered hexagonal boron nitride (h-BN), a wide bandgap 2D insulator consisting of alternating sp^2-boned boron and nitrogen atoms,[1,2] is of primary importance for functional devices based on 2D materials.[3–5] Settled on the atomically smooth and inert surface of h-BN, graphene can develop its peculiar ability and achieve its pristine high electronic mobility.[3,4] Sandwiched between h-BN layers, 2D materials such as graphene and transition metal dichalcogenides can form vertical van der Waals heterostructures to realize exceptional properties and excellent performance.[6–8] Taking h-BN as ultrathin dielectric tunneling barrier, graphene transistors with a high ON–OFF ratio have also been constructed.[5]

To construct these devices in large scale, continuous h-BN monolayer film has been successfully fabricated in large area on various metal substrates through chemical vapor deposition (CVD)[9–11] and cosegregation approach;[12] however, the obtained monolayer films mostly consist of coalesced h-BN domains with random orientations regardless that of the underlying substrates. This random in orientation would severely prohibit the uniform electrical performance of van der Waals heterostructure devices taking h-BN as the dielectric layer because the electronic properties of 2D-material-based devices have been proven to be ultrasensitive to their stacking orientations.[8,11] Furthermore, although the h-BN monolayer preserves outstanding properties including high in-plane mechanical strength and thermal conductivity comparable to that of graphene and excellent thermal stability higher than 900 °C in oxygen environment,[13–15] the inevitable disordered grain boundaries between neighboring h-BN domains with different orientations would introduce leakage of electricity and weaken its mechanical, thermal and chemical stabilities. On the other hand, it might be more important that a semiconductor surface can serve as a versatile platform for functional systems once covered by a perfect dielectric monolayer of h-BN.[16,17] Recently, graphene monolayer was epitaxially grown on germanium,[18] but aligned growth of h-BN monolayer on the surface of semiconductors still remains as a great challenge.

In this work, we realize the epitaxial growth of h-BN monolayer on both Ge (100) and Ge (110) surfaces with highly aligned orientations in large area for the first time. The h-BN monolayer can be facilely transferred without completely dissolving the Ge substrate and h-BN can be repeatedly grown on the Ge surface. The h-BN domains with the same orientation (coorientated domains) are shown to merge seamlessly by frictional force microscopy (FFM), while the boundaries between domains with opposite orientations (antiorientated domains) can be distinguished. Density functional calculations show that the local states contributed to the hexagonal-ring boundaries between antiorientated domains is distributed close to the band edge and the h-BN film can preserve its outstanding insulating property.

The growth of h-BN from the precursor of ammonia borane was conducted by using a low pressure CVD system as we described previously.[19,20] Placing the polished surface of the Ge wafer toward a flat quartz substrate can simply and efficiently suppress the evaporation of Ge at growing temperature (920 °C) close to its melting temperature (938.3 °C), which may coarsen the Ge surface seriously (Figure S1, Supporting Information). Although taking a high base pressure can also suppress the evaporation of Ge,[18] we found that h-BN cannot be deposited under the pressure of 100 Torr in our system. Typically, continuous h-BN films can be obtained by introducing the gas decomposition of ammonia borane to the furnace at 920 °C for 1 h (Figure S2, Supporting Information), during which the partial pressure of the gas decomposition was maintained at 0.5 Pa by modulating the temperature of the ammonia borane. The estimated domain size from Figure S2a (Supporting Information) is around 1 μm^2, which may be enlarged through reducing the partial pressure and introducing surface oxides of the substrate.[21,22]

J. Yin, X. Liu, J. Li, Y. Li, Y. Xu, X. Li, Prof. W. Guo
State Key Laboratory of Mechanics
and Control of Mechanical Structures
Key Laboratory for Intelligent Nano Materials and
Devices of the Ministry of Education
and Institute of Nanoscience
Nanjing University of Aeronautics and Astronautics
Nanjing 210016, China
E-mail: wlguo@nuaa.edu.cn

W. Lu, Prof. C. Jin
State Key Laboratory of Silicon Materials
School of Materials Science and Engineering
Zhejiang University
Hangzhou 310027, China

Y. Cao, Prof. J. Zhou
Wuhan National Laboratory for Optoelectronics
and College of Optoelectronic Science and Engineering
Huazhong University of Science and Technology
Wuhan 430074, China

DOI: 10.1002/smll.201501439

© 2015 Wiley-VCH Verlag GmbH & Co. KGaA, Weinheim

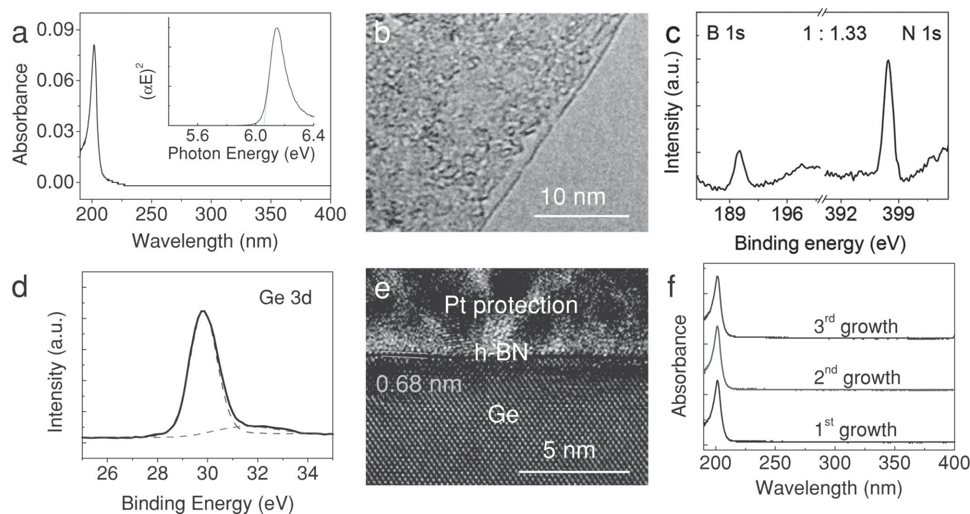

Figure 1. Growth of h-BN monolayer on reusable Ge. a) UV–vis spectrum of a monolayer h-BN film. Inset shows the deduced optical bandgap. b) TEM image at the edge of an h-BN film. c) B 1s and N 1s XPS spectra of h-BN on Ge and the deduced atom ratio of B to N. d) Ge 3d XPS spectra of the sample. e) High-resolution TEM image of the cross section of the h-BN on Ge. f) UV–vis spectrum of three h-BN films subsequently grown on the same Ge substrate.

The h-BN film was characterized by UV–vis absorption spectrum. As shown in **Figure 1**a, the h-BN film transferred onto a transparent quartz substrate exhibits zero absorbance in the visible-light range and only a sharp absorption peak at 202 nm, showing the typical characteristic of h-BN. The deduced optical bandgap according to the formula for a direct band semiconductor is 6.06 eV (inset of Figure 1a).[23] This value is larger than that of few-layered h-BN and consistent with that for monolayer predicted theoretically and measured experimentally,[24,25] indicating that the h-BN film is monolayer. The layer number of the h-BN film was further confirmed by the transmission electron microscopy (TEM) image taken at the edge of the h-BN film, as shown in Figure 1b. The thickness of h-BN is uniform in large area, as confirmed by the uniform contrast in the scanning electron microscopy image of continuous h-BN on Ge (Figure S2b, Supporting Information).

X-ray photoemission spectroscopy (XPS) was also performed on the as-grown h-BN film on Ge to determine the chemical composition of the sample. As shown in Figure 1c, the B 1s peak and N 1s peak are located at 190.3 and 397.8 eV, respectively, consistent with the values reported previously for h-BN.[10] However, the deduced B/N ratio is 1:1.33, severely deviating from the ideal 1:1 ratio. We attribute this large deviation to the nitridation of the Ge surface, as confirmed by the XPS spectra of the Ge 3d peak shown in Figure 1d. Besides the peak at 29.8 eV contributed to elementary Ge, another peak at 31.6 eV corresponding to Ge—N bond shows up.[26] Actually, it is reasonable to detect the nitridation of the Ge surface for our sample because the NH_3 gas in the decomposition of ammonia borane would react with Ge to form Ge_3N_4 at temperature above 300 °C.[26] However, for the evaporation of Ge_3N_4 at temperature above 600 °C in vacuum,[26] it is much likely that only the surface atoms of the Ge wafer was nitrified, without a layer of bulk Ge_3N_4 structure between the h-BN and Ge. The nitridation of Ge surface is further confirmed by a much smaller B/N ratio (1:2.30) of a Ge sample partially covered with h-BN (Figure S3, Supporting Information).

Contributed to the passivation of the Ge surface, it is found that the interface distance between h-BN and the nitrogen-terminated Ge surface is around 0.68 nm (Figure 1e), larger than both the interlayer distance of h-BN (0.33 nm) and the measured lattice constant of Ge (0.51 nm, Figure S4, Supporting Information) perpendicular to the surface. The large interface distance implies a weak interaction between the nitrogen-terminated Ge substrate and h-BN. This may be the origin that the h-BN can be detached from the Ge substrate, which can be then recycled for repeated growth of h-BN. To transfer the h-BN, the polymethyl methacrylate (PMMA) coated h-BN film was first detached from the Ge substrate through intercalating an aqueous solution of NaOH and H_2O_2, and then loaded onto a target substrate (see the Experimental Section for details). Compared to the transfer method described by Lee et al. for graphene,[18] which takes Au as the mediate support film, this method avoids the use of noble metals and therefore is much more cost efficient. We repeated the h-BN growth-detaching cycle for three times on the same Ge substrate. UV–vis spectra of the h-BN transferred onto transparent quartz shows almost identical features for all the h-BN without degradation, demonstrating the stability and high quality of the h-BN grown on the reusable Ge substrate.

To explore the orientations of h-BN domains, we reduced the growth duration to 30 min to prevent the fully merging of the neighbor h-BN domains. The topography and orientations of h-BN domains with partial coverage can be revealed facilely by FFM for the ultralow friction character of perfect h-BN monolayer (Figure S5, Supporting Information).[20] As shown in **Figure 2**a, h-BN domains grown on Ge (110) exhibit nearly equilateral triangles. Selected-area electron diffraction (SAED) of a single h-BN domain supported on an amorphous carbon film (Figure 2b) indicates that the triangle domain is single crystal and the edges of the

© 2015 Wiley-VCH Verlag GmbH & Co. KGaA, Weinheim

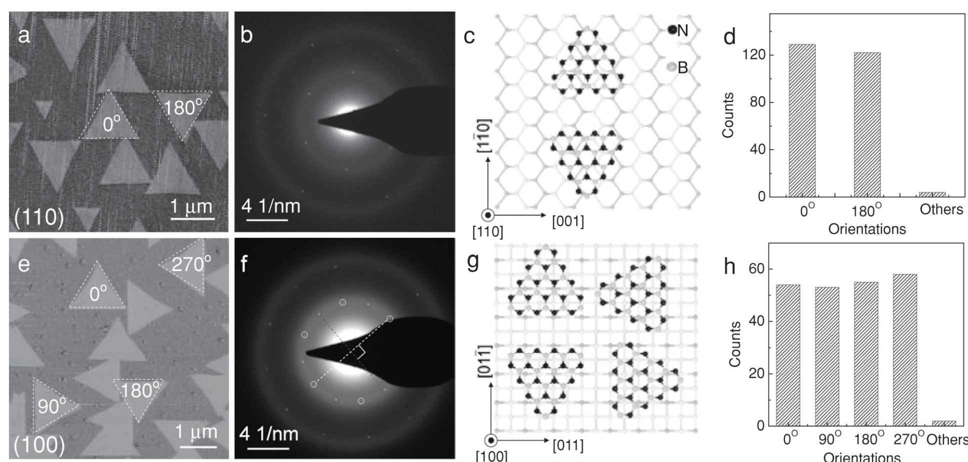

Figure 2. The orientations of h-BN domains grown on Ge (110) and Ge (100). Friction force images of h-BN domains grown on Ge (110) a) and Ge (100) e), respectively. The dashed equilateral triangles highlight the typical orientations of the h-BN domains. SAED patterns taken at regions including one triangle supported on carbon film b) and triangles perpendicular to each other f). c,g) Schematic illustration of the deduced orientations of the h-BN domains with respect to the underlying Ge (110) e) and (100) j) substrates, with a measurement variation less than ±2°. Statistical distribution of the orientations of the h-BN domains grown on Ge (110) d) and Ge (100) h), respectively.

triangle are along the zigzag orientation of the h-BN lattice (Figure S6, Supporting Information), in consistent with previous results that h-BN triangles are prone to N-terminated zigzag edges.[27,28] Then, according to the edge orientation of the epitaxial h-BN triangles relative to the cleavage orientation (edges) of Ge (110) substrate (Figure S7, Supporting Information), it can be deduced that one N-terminated zigzag edge of the h-BN triangles is orientated along either 0° or 180° to the [001] crystal orientation of the Ge (110) substrate (Figure 2c). Based on the orientation, the h-BN triangles are then categorized to 0° and 180° domains, respectively, as marked in Figure 2a. Thus, 0° and 180° h-BN domains are of atom lattices mirror to each other, analog to the antiphase phenomenon in traditional polar-on-nonpolor epitaxy,[29] and only one set of diffraction spots with sixfold symmetry appear for a region involving two antiorientated domains (Figure S8, Supporting Information). Examinations of several random locations spaced larger than 5 mm shows the similar situation, indicating that the h-BN domains are highly aligned in a large area (Figure S9, Supporting Information). Statistics demonstrate that the percentage of h-BN domains aligned along these two orientations exceeds 98% and the numbers of h-BN domains categorized to each direction are comparable (Figure 2d). Topography and friction force images (Figure S10, Supporting Information) of a domain in orientation deviated from 0° or 180° demonstrate that the nucleation of these domains is mainly disturbed by contaminations, and the percentage of the aligned h-BN domains could be further improved by optimizing the clean process to reduce the surface contaminants.

Although epitaxial growth of graphene on Ge is confined to the (110) surface,[18] h-BN triangles grown on Ge (100) surface are also highly aligned (Figure 2e). However, two groups of antiorientated domains with edges perpendicular to each other are observed. As we have discussed above, perpendicular edges indicate perpendicular lattice orientations as well, which is confirmed by the two sets of diffraction spots with a rotation angle of 90° (Figure 2f). The orientation of the epitaxial h-BN with respect to the underlying Ge (100) was also determined as shown in Figure 2g. On the Ge (100) surface, one N-terminated zigzag edge of the h-BN triangles is either parallel or perpendicular to the [011] crystal orientation of the Ge substrate. Based on that, the h-BN domains are classified to 0°, 90°, 180°, and 270° orientated ones (Figure 2e), respectively, and the ratio of h-BN domains cataloged to each orientation is very close (Figure 2h). The h-BN domains in orientations deviated from the primary orientations contribute less than 1% of all the h-BN domains.

Based on these results, it can be concluded that the number of primary orientations for epitaxial h-BN on different crystal faces of Ge has close relationship to the symmetry of the Ge surface. The Ge (110) surface preserves twofold symmetry (Figure 2e), which provides two equivalent preferred orientations for the nucleation of h-BN with orientations opposite to each other. The fourfold symmetry of Ge (100) surface doubles the equivalent preferred nucleation orientations compared to that of Ge (110) surface, and two groups of h-BN antiorientated domains perpendicular to each other appears.

Furthermore, the merging boundaries between coorientated and antiorientated h-BN triangles were examined. We find that FFM images can be applied to clearly distinguish the merging boundaries between antiorientated domains, as shown in **Figure 3**a,b. It can be seen that antiorientated domains can merge both along the twin-boundary and tilt-boundary directions at the microscale. Figure 3a shows that two antiorientated domains merge along two different zigzag orientations at the microscale, tending to form three straight twin boundaries. A couple of tilt-boundary lines, which orientate along 165° to one free edge of the triangle, are shown in Figure 3b. The merging boundaries between perpendicularly orientated domains can also be distinguished, as shown in Figure S11 (Supporting Information). However, no notable boundary is found between h-BN domains merging with the same orientation, as shown in Figure 3c. This can be seen more obviously in Figure 3d, where an h-BN domain merges

© 2015 Wiley-VCH Verlag GmbH & Co. KGaA, Weinheim

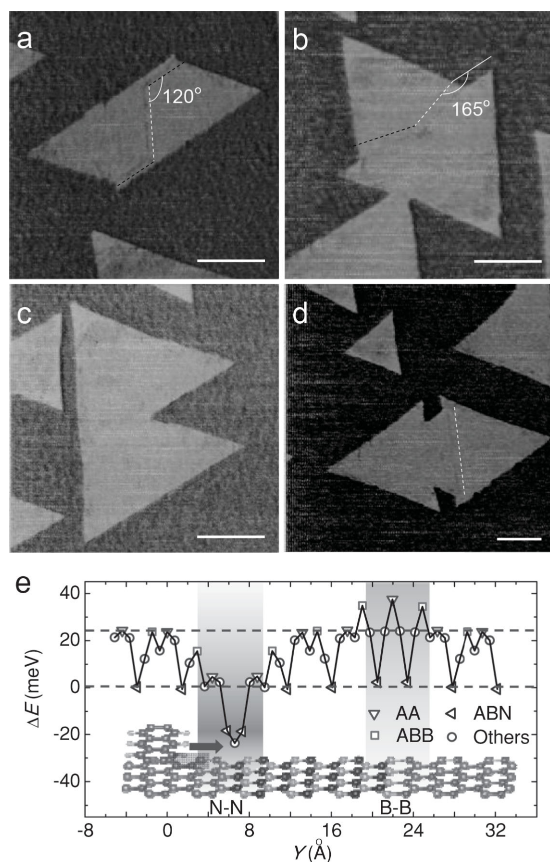

Figure 3. Merging boundaries between coorientated and anti-orienatated domains. High-magnified friction images of aggregates of h-BN triangles with opposite a,b), the same c), and both opposite and the same d) orientations. The dashed lines mark where the frictional signals show notable boundaries between two domains with a small offset. Scale bar: 0.5 μm. e) The energy corrugation of sliding a GNR across the N—N and B—B seamless grain boundaries. Inset shows the simulation models.

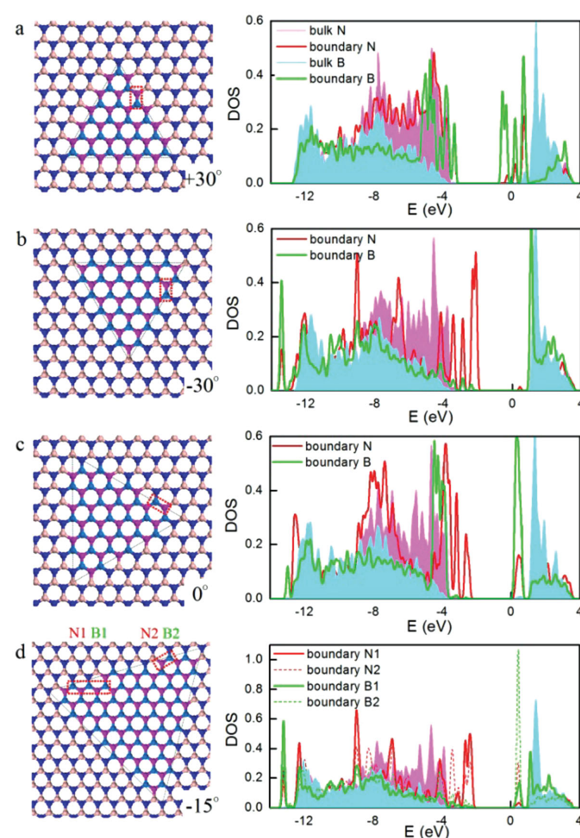

Figure 4. Structures and electrical properties of ideal antiorientated grain boundaries. Periodic super cell model (left panels) and density of states (right panels) of 30° B—B zigzag boundary a), −30° N—N zigzag boundary b), 0° armchair boundary c), and −15° tilt boundary d). The dashed red squares in the structure model mark the boundary atoms, which cause the localized states shown in the right.

with a coorientated domain at the left side and another anti-orientated domain at the right side, and only the merging boundary between antiorientated domains shows notable contrast in the FFM image. This notable difference highly implies that coorientated h-BN domains merge seamlessly.

The enhanced friction force for the boundaries between antiorientated domains is reasonable when considering the boundary induced local states, even if the antiorientated domains merge seamlessly with hexagon rings. Our simulation of sliding a graphene nano ribbon (GNR) across seamless B—B and N—N grain boundaries shows an enhanced energy corrugation contributed to the boundaries. As shown in Figure 3e, the energy corrugation of sliding the GNR across perfect h-BN lattice is only around 24 meV for a unit cell, where AA (eclipsed with C over both B and N) and ABN (staggered with C over B) stacking have the maximum and the minimum energy, respectively. When the GNR layer slides across the N—N (B—B) boundary as highlighted by the blue (red) shade, an extremely low (high) stacking energy appears which gives a much higher energy corrugation of 48 meV (37 meV) for a unit cell. Thus, the friction force across the N—N (B—B) boundary is evaluated to be increased by 100% (54%), as the maximum friction is proportional to the energy corrugation according to the Tomlinson model.[30]

Atomic resolution examination of the grain boundaries is greatly challenged at this stage for the difficulty of distinguishing B and N atoms and the fragility of h-BN under high-energy e-beam irradiation.[31] To give some prior evaluation of the electrical property of the h-BN film with antiorientated boundaries, we perform density functional theory (DFT) calculations on the structure of the ideal boundaries bridging antiorientated domains, which are supposed to be perfect hexagon rings with homogenous bonds. The boundaries between antiorientated domains can be classified into four types, i.e., zigzag along the N-terminated edge (**Figure 4**a, analog to the boundaries in Figure 3a,d marked by white lines), zigzag along the B-terminated edge (Figure 4b, analog to the boundaries in Figure 3a marked by black lines), armchair (Figure 4c), and tilt (Figure 4d, analog to the boundaries in Figure 3b marked by white line) types. For a general denotation, the zigzag boundaries along the N-terminated edge and B-terminated edge are labeled as 30° and −30° (Figure 4a,b) respectively, the armchair boundary is labeled as 0°, and the remains orientations can take angles between −30° and 30°. The main consequence of the boundaries is to arouse localized states among the bulk gap. By plotting the charge density distribution of the localized states, it is found

© 2015 Wiley-VCH Verlag GmbH & Co. KGaA, Weinheim

that in the 30° boundary, the localized states under the Fermi level is mainly π-like states in N atoms, due to the excess of *p* electron in N. In the case of –30° boundary, the occupied and unoccupied localized states are σ-like states and π-like states of B—B bond, respectively. As 0° and ≈15° boundaries have both homoelemental N—N and B—B bonds, both those localized states can be observed. However, all the localized states are found to distribute close to the bulk band edge and the bandgap are still up to 2.3 eV for –30° boundary and 2.8 eV for 30° boundary. Considering the underestimation of gap by Perdew–Burke–Ernzerhof (PBE) functional, the boundaries should still preserved an excellent insulating property.

It is need to note that the real situation of antiorientated boundaries can be more complicated. Although the straight boundaries along the N—N/B—B zigzag direction or with an rotation angle of 165° are observed at the microscale, they can consist of polylines of variable orientations at atomic scale, similar to the case reveled in MoS_2 grown by CVD.[32] Besides, pentagon–octagon–pentagon and nonpolar square–octagon line defects were also proposed for antiorientated h-BN domains,[33,34] although with a higher distortion strain energy.

In conclusion, by using low pressure CVD, we successfully obtained highly aligned h-BN monolayer of high quality in large area on reusable germanium surface. The number of primary orientations of the h-BN domains shows notable dependence on the symmetry of the underlying crystal face. On Ge (110) surface, only coorientated and antiorientated h-BN domains are found. Coorientated h-BN domains are shown to merge seamlessly by FFM, while merging boundaries between antiorientated domains are clearly distinguished. Although localized states contributed to hexagon-rings boundaries between antiorientated domains arise, the h-BN film still preserves a large electrical bandgap.

Experimental Section

Synthesis of h-BN: The Ge substrates (0.5 mm thick, undoped) were cut along the cleavage orientations into small pieces and then dipped into 10% diluted hydrofluoric acid (HF) to remove the native oxide. Once the Ge substrates were taken out from the HF solution, they were immediately loaded into a CVD chamber, which was then evacuated down to 0.1 Pa to prevent the reoxidization of the Ge surface. After the chamber was flushed with a 9 sccm H_2 at 90 Pa for 1 h, it was heated to 920 °C in 1 h and maintained at this temperature for the deposition of h-BN. To synthesize h-BN, the borazane power was heated in an isolated container to raise the gas pressure by 0.5 Pa.[19,20] Finally, the chamber was rapidly cooled down to room temperature after the desired growth time.

Transfer of h-BN: The h-BN film was transferred onto the target substrates by a PMMA-assisted transfer method and the underlying Ge substrate can be reused to grow h-BN repeatedly. First, a thin film of PMMA was spin coated onto the h-BN/Ge and then curved at 120 °C for 10 min. Afterward, the sample was floated on the surface of an aqueous solution (100 mL 8 wt % NaOH and 10 mL H_2O_2). After around 10 min, the PMMA/h-BN film would be detached from the Ge substrate automatically and the underlying Ge substrate would sink to the bottom. After the PMMA/h-BN film was rinsed with deionized water for several cycles, it was loaded by a target substrate and then annealed at 150 °C for 10 min to improve the adhesion between the film and the substrate. Finally, PMMA was dissolved with hot acetone, and the sample was annealed under 10 sccm hydrogen at 600 °C for 2 h to remove the possible residual contamination.

Friction Force Simulation: DFT calculation including vdW-DF,[35] which approximately accounts for dispersion interactions, as implemented in the Vienna ab initio simulation package (VASP),[35,36] is employed to calculate the atomic and electronic structures and energies of our systems. The projector-augmented wave (PAW) method and PBE functional are used for pseudo potential and the exchange correlation. The cutoff energy is 500 eV. The energies and the forces are calculated to converge to the accuracy of 1.0×10^{-4} eV and 0.01 eV $Å^{-1}$, respectively. The size of the optimized cell is 2.510 × 30.723 Å in the *x*–*y* plane and with a length of 30 Å in the *z*-direction, leaving a vacuum region of more than 15 Å. The optimized B—N bond is 1.45 Å, the B—B bond is 1.72 Å, and the N—N bond is 1.43 Å.

Electrical Property Analysis: The DFT calculations were performed by VASP code,[36,37] using the PAW method for pseudo potential and PBE functional for the exchange correlation. The conjugate gradient method was used to fully relax the geometry until the force on each atom is less than 0.01 eV $Å^{-1}$. The idealized boundaries are simulated by exchanging the B and N atoms located in a triangle area of a perfect BN lattice (the left panel of Figure 4), giving the opportunity to reveal the properties of one kind of boundary in each model.[38]

Supporting Information

Supporting Information is available from the Wiley Online Library or from the author.

Acknowledgements

This work was supported by 973 program (Grant Nos. 2013CB932604 and 2012CB933403), the National and Jiangsu Province Science Foundation (Grant Nos. 51472117 and BK20130781) of China, the Research Fund of State Key Laboratory of Mechanics and Control of Mechanical Structures (0414K01), the NUAA Fundamental Research Funds (NP2015203), and a Project Funded by the Priority Academic Program Development of Jiangsu Higher Education Institutions.

[1] R. S. Pease, *Nature* **1950**, *165*, 722.
[2] K. Watanabe, T. Taniguchi, H. Kanda, *Nat. Mater.* **2004**, *3*, 404.
[3] C. R. Dean, A. F. Young, I. Meric, C. Lee, L. Wang, S. Sorgenfrei, K. Watanabe, T. Taniguchi, P. Kim, K. L. Shepard, J. Hone, *Nat. Nanotech.* **2010**, *5*, 722.
[4] J. Xue, J. Sanchez-Yamagishi, D. Bulmash, P. Jacquod, A. Deshpande, K. Watanabe, T. Taniguchi, P. Jarillo-Herrero, B. J. LeRoy, *Nat. Mater.* **2011**, *10*, 282.
[5] L. Britnell, R. V. Gorbachev, R. Jalil, B. D. Belle, F. Schedin, A. Mishchenko, T. Georgiou, M. I. Katsnelson, L. Eaves,

© 2015 Wiley-VCH Verlag GmbH & Co. KGaA, Weinheim

S. V. Morozov, N. M. R. Peres, J. Leist, A. K. Geim, K. S. Novoselov, L. A. Ponomarenko, *Science* **2012**, *335*, 947.
[6] J. Yu, W. Guo, *J. Phys. Chem. Lett.* **2013**, *4*, 951.
[7] F. Withers, O. Del Pozo-Zamudio, A. Mishchenko, A. P. Rooney, A. Gholinia, K. Watanabe, T. Taniguchi, S. J. Haigh, A. K. Geim, A. I. Tartakovskii, K. S. Novoselov, *Nat. Mater.* **2015**, *14*, 301.
[8] C. R. Dean, L. Wang, P. Maher, C. Forsythe, F. Ghahari, Y. Gao, J. Katoch, M. Ishigami, P. Moon, M. Koshino, T. Taniguchi, K. Watanabe, K. L. Shepard, J. Hone, P. Kim, *Nature* **2013**, *497*, 598.
[9] K. K. Kim, A. Hsu, X. Jia, S. M. Kim, Y. Shi, M. Hofmann, D. Nezich, J. F. Rodriguez-Nieva, M. Dresselhaus, T. Palacios, J. Kong, *Nano Lett.* **2012**, *12*, 161.
[10] L. Wang, B. Wu, J. Chen, H. Liu, P. Hu, Y. Liu, *Adv. Mater.* **2014**, *26*, 1559.
[11] W. Yang, G. Chen, Z. Shi, C.-C. Liu, L. Zhang, G. Xie, M. Cheng, D. Wang, R. Yang, D. Shi, K. Watanabe, T. Taniguchi, Y. Yao, Y. Zhang, G. Zhang, *Nat. Mater.* **2013**, *12*, 792.
[12] C. Zhang, L. Fu, S. Zhao, Y. Zhou, H. Peng, Z. Liu, *Adv. Mater.* **2014**, *26*, 1776.
[13] L. H. Li, J. Cervenka, K. Watanabe, T. Taniguchi, Y. Chen, *ACS Nano* **2014**, *8*, 1457.
[14] D. Golberg, Y. Bando, Y. Huang, T. Terao, M. Mitome, C. Tang, C. Zhi, *ACS Nano* **2010**, *4*, 2979.
[15] I. Jo, M. T. Pettes, J. Kim, K. Watanabe, T. Taniguchi, Z. Yao, L. Shi, *Nano Lett.* **2013**, *13*, 550.
[16] D. A. Muller, T. Sorsch, S. Moccio, F. H. Baumann, K. Evans-Lutterodt, G. Timp, *Nature* **1999**, *399*, 758.
[17] H. Yang, J. Heo, S. Park, H. J. Song, D. H. Seo, K.-E. Byun, P. Kim, I. Yoo, H.-J. Chung, K. Kim, *Science* **2012**, *336*, 1140.
[18] J.-H. Lee, E. K. Lee, W.-J. Joo, Y. Jang, B.-S. Kim, J. Y. Lim, S.-H. Choi, S. J. Ahn, J. R. Ahn, M.-H. Park, C.-W. Yang, B. L. Choi, S.-W. Hwang, D. Whang, *Science* **2014**, *344*, 286.
[19] J. Yin, X. Li, J. Zhou, W. Guo, *Nano Lett.* **2013**, *13*, 3232.
[20] X. Li, J. Yin, J. Zhou, W. Guo, *Nanotechnology* **2014**, *25*, 105701.
[21] Y. Hao, M. S. Bharathi, L. Wang, Y. Liu, H. Chen, S. Nie, X. Wang, H. Chou, C. Tan, B. Fallahazad, H. Ramanarayan, C. W. Magnuson, E. Tutuc, B. I. Yakobson, K. F. McCarty, Y.-W. Zhang, P. Kim, J. Hone, L. Colombo, R. S. Ruoff, *Science* **2013**, *342*, 720.
[22] J. Yin, J. Yu, X. Li, J. Li, J. Zhou, Z. Zhang, W. Guo, *Small* **2015**, DOI: 10.1002/smll.201500210.
[23] W. Baronian, *Mater. Res. Bull.* **1972**, *7*, 119.
[24] X. Blase, A. Rubio, S. G. Louie, M. L. Cohen, *Phys. Rev. B* **1995**, *51*, 6868.
[25] Y. Gao, W. Ren, T. Ma, Z. Liu, Y. Zhang, W.-B. Liu, L.-P. Ma, X. Ma, H.-M. Cheng, *ACS Nano* **2013**, *7*, 5199.
[26] S. J. Wang, J. W. Chai, J. S. Pan, A. C. H. Huan, *Appl. Phys. Lett.* **2006**, *89*, 022105.
[27] W. Auwärter, M. Muntwiler, J. Osterwalder, T. Greber, *Surf. Sci.* **2003**, *545*, L735.
[28] W. Auwärter, H. U. Suter, H. Sachdev, T. Greber, *Chem. Mater.* **2004**, *16*, 343.
[29] H. Kroemer, *J. Cryst. Growth* **1987**, *81*, 193.
[30] A. Socoliuc, R. Bennewitz, E. Gnecco, E. Meyer, *Phys. Rev. Lett.* **2004**, *92*, 134301.
[31] J. Kotakoski, C. H. Jin, O. Lehtinen, K. Suenaga, A. V. Krasheninnikov, *Phys. Rev. B* **2010**, *82*, 113404.
[32] A. M. van der Zande, P. Y. Huang, D. A. Chenet, T. C. Berkelbach, Y. You, G.-H. Lee, T. F. Heinz, D. R. Reichman, D. A. Muller, J. C. Hone, *Nat. Mater.* **2013**, *12*, 554.
[33] X. Li, X. Wu, X. C. Zeng, J. Yang, *ACS Nano* **2012**, *6*, 4104.
[34] Y. Liu, X. Zou, B. I. Yakobson, *ACS Nano* **2012**, *6*, 7053.
[35] M. Dion, H. Rydberg, E. Schröder, D. C. Langreth, B. I. Lundqvist, *Phys. Rev. Lett.* **2004**, *92*, 246401.
[36] G. Kresse, J. Hafner, *Phys. Rev. B* **1994**, *49*, 14251.
[37] G. Kresse, J. Furthmüller, *Phys. Rev. B* **1996**, *54*, 11169.
[38] Y. Liu, S. Bhowmick, B. I. Yakobson, *Nano Lett.* **2011**, *11*, 3113.

Received: May 21, 2015
Revised: June 14, 2015
Published online: August 26, 2015

© 2015 Wiley-VCH Verlag GmbH & Co. KGaA, Weinheim